System and Component Development for Long-Duration Energy Storage Using Particle Thermal Energy Storage

Zhiwen Ma[1,*], Xingchao Wang[1,4], Patrick Davenport[1], Jeffrey Gifford[1,4], Korey Cook[1], Janna Martinek[1], Jason Schirck[2], Aaron Morris[2], Matthew Lambert[3], and Ruichong Zhang[4]

[1]National Renewable Energy Laboratory, 15013 Denver West Parkway, Golden, CO80401
[2]Purdue University, [3]Allied Mineral Products, Inc., [4]Colorado School of Mines
[*]Phone number: 303-275-3784, e-mail address: zhiwen.ma@nrel.gov

Abstract

Energy storage, at various scales, will be required to maintain reliable power supply from variable renewable resources, and improve grid resilience. Long-duration energy storage (10–100 hours) can substitute baseload coal power generation and increase levels of renewable power supply. Thermal energy storage (TES) has siting flexibility and the ability to store a large capacity of energy, and thus it has the potential to meet the needs of long-duration energy storage. A novel TES system was developed by using solid particles as storage media and charging/discharging electricity from renewable power connected via the electric grid. The particle TES uses low-cost silica sand at 30–40$/Ton that is stable at high temperatures of greater than 1,000°C. Thus, the particle TES system has an overall low storage cost and high thermal-power efficiency. Key components of the system were conceptually designed and modeled for their performance. Conversion of electricity to thermal energy using electric heating can achieve a greater than 98% charging efficiency, and the conversion of thermal energy back to electricity uses an air-Brayton combined power cycle with >52% thermal-to-electricity efficiency at >1,170°C to achieve a >50% roundtrip efficiency after subtracting estimated plant parasitic losses. Laboratory-scale prototypes were fabricated and tested to verify their design approaches and operations relevant to product-scale components.

Keywords: thermal energy storage, electric-thermal energy storage, solid particles, renewable energy, long-duration energy storage

Highlights

- A novel electric-thermal energy storage system is introduced to serve long-duration energy storage.
- Low-cost, stable silica sand is used as storage media for economic grid electricity storage.
- Designs and the prototype development of major components are presented.
- Product-scale modeling and prototype testing show component and system feasibility.

Graphic Abstract

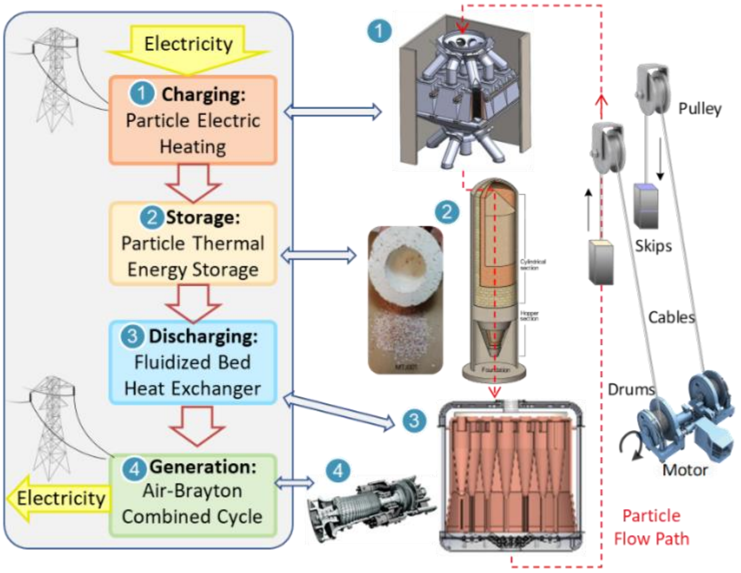

Electric-Thermal Energy Storage and Component Concepts
(See Figures 1 and 2, Table 3 for details)

1. Introduction

Greatly increasing renewable generation integration and reducing fossil fuel usage is a path to decarbonize the energy supply. The rapid growth of renewable energy increases the importance of economically firming the electricity supply from variable solar photovoltaic and wind power generators. Energy storage will be key to manage variability and to bridge the generation gap over timescales of hours or days for high levels of renewable generation grid integration [1]. The integration of storage for excess electricity from renewable sources has several significant and positive impacts, including: (1) reducing curtailment and expanding the proportion of the total electricity generation supplied by renewable sources, (2) improving grid reliability and peak-load response, and (3) providing electricity supply to meet demand [2]. Long-duration energy storage (LDES), with 10–100 hours of discharge capacity, can complement the reduction of fossil fuel baseload generation and mitigate the risks to grid reliability when a large portion of electricity comes from variable renewable sources [3].

Several energy storage methods are deployed or under development, including mechanical, chemical, electrochemical, and thermal energy storage (TES). Recently, Schmidt et al. studied the levelized cost of storage (LCOS) of nine technologies and 12 power system applications, including compressed air energy storage (CAES); pumped storage hydropower (PSH); hydrogen; flywheel; supercapacitor; and various battery types including redox flow batteries, sodium-sulfur, lead-acid, and lithium batteries [4]. The study indicated that most technologies currently have a LCOS range of 150–600 US$/MWh in 2015 and projected cost of $130–200

US$/MWh in 2050 based on a $50/MWh charging electricity price [4]. Without significantly high fuel prices or policy support, such as a carbon tax, it would be difficult for storage at this cost range to compete with cheap natural gas for baseload power supply. Reducing input renewable electricity price is key to lower LCOS in a competitive range. Additionally, reducing storage technology cost is critical to make LDES economically viable to displace fossil fuels.

No single storage technology can yet cover all electricity storage needs to achieve a carbon-free utility target. TES technology has the potential to be low cost, has no geographic siting restrictions, and can be employed in various configurations for electricity storage. TES technology had been developed and commercially deployed with concentrating solar power (CSP); however, TES for grid-scale electricity storage is a lesser known technology option and therefore is often inadequately analyzed in comparison to other energy storage technologies, such as the LCOS studies by Schmidt et al. [4].

Thermal energy storage covers broad material types and applications in power and heat supply [5]. We particularly investigated TES systems suitable for grid-scale energy storage and focused on solid particle-based TES to serve the LDES purpose. TES can be integrated in grid-scale energy storage via applications including CSP [6], nuclear [7,8], and grid-tied, stand-alone electric-thermal energy storage (ETES). Historically TES has often been developed alongside CSP technology; however, a standalone TES for grid-scale energy storage does not need a CSP mirror field for solar energy collection and conversion and can be independent from a CSP plant. TES development as a stand-alone ETES system broadens potential applications for TES to integrate renewable energy from solar photovoltaic and wind power [9]. Compared with LDES alternatives—such as PSH, CAES, and chemical storage technologies such as green hydrogen—TES has a low storage cost and can be sited adjacent to end users, with minimal geographic constraints [10].

Energy storage cost and performance are critical to viable storage economics, particularly for long-duration storage applications. LDES methods—including TES, thermochemical energy storage, pumped thermal energy storage, and flow batteries—are under development with support from the U.S. Department of Energy Advanced Research Projects Agency–Energy (ARPA-E) Duration Addition to electricitY Storage (DAYS) program [11]. This paper presents the technology development on a grid-scale ETES system for LDES applications. The particle-based ETES system uses particle TES that can reduce capital costs while operating at high temperatures and in a wide temperature range of from <-100°C to >1,000°C [10]. Grid-scale systems in the TES category have low round-trip electric conversion efficiencies (~50%)

compared to PSH or batteries [12], despite high thermal storage efficiency, meaning there is margin for improvement. Towards commercialization, Siemens Gamesa and Malta [13] have worked on pilot TES plants to prove TES at scale. The particle ETES system is aimed at facilitating future high renewable integration into the grid with low-cost and large-capacity energy storage.

A particle ETES configuration is shown conceptually in Figure 1. During off-peak hours, when electric power is cheapest, the low temperature particles are transported to the top of the particle lifter and fall through the electric particle heater, thereby charging the storage modules using direct electric resistance heating powered by renewable electricity. The hot particles are stored in containment silos with internal refractory insulation. At peak power demand at a high electricity price, the hot particles move through a heat exchanger to discharge the stored thermal energy and heat a working fluid that drives a high-efficiency air-Brayton combined-cycle (ABCC) power system attached to an electric generator, to convert stored thermal energy back to electricity.

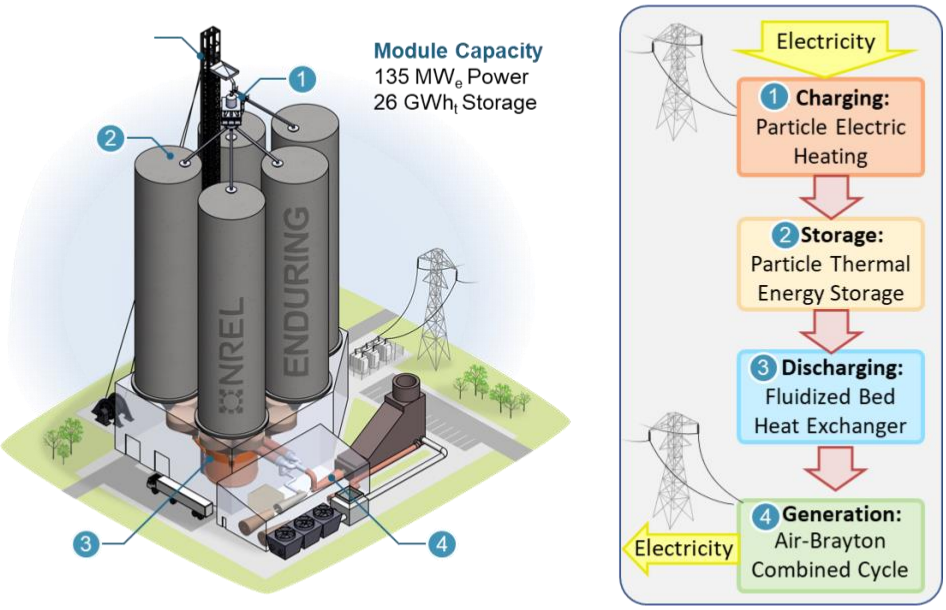

Figure 1. A configuration of a particle ETES system based on an air-Brayton combined-cycle for thermal electricity generation.

Unlike TES in conventional molten salt CSP systems [14], the particle ETES system uses solid particles as the storage media, similar to the development of a low-cost, high-temperature, particle-based Generation 3 CSP system [15], but it uses grid connection to charge and discharge electricity without a CSP field as the energy flow chart shown in Figure 1. The stand-alone ETES system avoids a solar field and the siting limitations of CSP deployment that requires high solar irradiation. ETES has scaling and siting flexibility to support the integration of grid-scale renewable power and other thermal energy supplies.

A key consideration for ETES is to maximize thermal cycle efficiency through cycle designs and operating conditions. The simple conversion of electricity to thermal energy using electric heating can achieve a greater than 98% charging efficiency, and the conversion of thermal energy back to electricity uses an ABCC power cycle with >52% thermal-to-electricity efficiency at >1,170°C to achieve a >50% round-trip efficiency after subtracting an estimated amount of plant parasitic losses. A particle ETES system enables high storage and high working-fluid temperatures to support high efficiency of thermal power cycles while maintaining low storage costs.

System and component development has yielded feasible designs and is currently in the stage of testing prototypes. Various modeling tools were developed to study different component designs and performance and to simulate system performance. Major technology challenges ahead include pilot validation of component designs, fabrication, performance, operability, and system integration for various application configurations. Recent progresses in the modeling and testing of major components have shown the technical feasibility of the particle ETES system for LDES applications.

2. Particle ETES System and Components

Particle ETES Configuration

The particle ETES system includes an electric charging particle heater, TES modules, skip hoists for transporting particles, a pressurized fluidized bed (PFB) heat exchanger (HX), and a high-performance ABCC power generation. Figure 2 shows the storage process, energy flow, and air and particle flow paths through charging and discharging components. The ABCC power cycle, as shown in Figure 2 and elaborated in Section 3.4, provides the operating parameters that determine the charging/discharging components and storage capacity. The PFB HX is based on the configuration of commercial PFB combustion boilers [16] and has an inner hot fluidized bed for air/particle direct contact heat transfer surrounded by an external pressure vessel to hold the air pressure. The ABCC power system is adopted from a commercial gas turbine combined cycle (GTCC) system by substituting gas combustors with hot air passages connected with the PFB HX. The high-pressure air from the turbine compressor contacts the hot particles, which are fed through the PFB HX and heated to the turbine inlet temperature. The hot air then flows through the turbine and drives a power generator. The turbine exhaust hot air flows through a heat recovery steam generator that drives a bottom steam Rankine power cycle. Current work investigated the particle ETES system and major components through conceptual designs, performance modeling, and prototype testing.

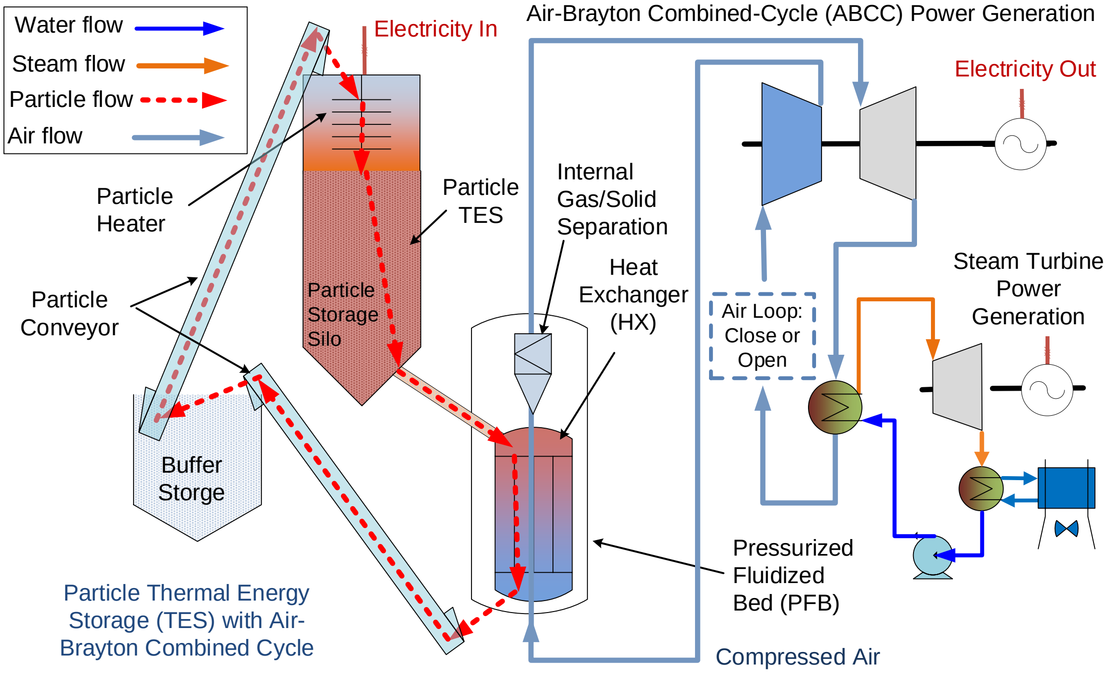

Figure 2. System flow diagram and storage configuration using particle TES with ABCC power generation for ETES.

System and Component Specifications for TES Development

The specifications for the system diagram shown in Figure 1 are listed in Table 1 and serve as design conditions for component sizing and configurations. Component designs are based on heat/mass balances for the electric heater, particle TES, PFB HX, and auxiliary equipment, including particle transport and compressed air connections with the power block. The power-specific components include the power blocks and the components for energy conversion, including the PFB HX.

Figure 1 and Figure 1 show the energy flow path carried by hot particles heated by the charging electric heater (1) into the storage silo (2). When discharging, hot particles flow through a lock hopper to isolate the storage silo at ambient pressure from the PFB HX. Particles first fill the lock hopper container, and then the lock hopper is pressurized to an equal pressure to the PFB HX and releases particles into PFB HX gravitationally. Two such lock hoppers operate alternatively to maintain continuous particle flow to the PFB HX. Lock hopper is a conventional device that has been developed in Integrated Gasification Combined Cycle technology and applied broadly in process engineering and plants.

Many ways to dispense particles from a pressurized heat exchanger to seal hot air have been developed or used in industry. A few examples include lock hopper as described for the particle inlets, rotary valves, or loop seals for fluidized beds. The industry practice uses particles to seal air, and it is possible to dispense particles without leaking air other than air entrained by particles. The current consideration for low-temperature particles exiting the heat exchanger uses a pressure regulation rotary valve and transport to a buffer silo.

Table 1. Specification of commercial-scale system and components

Items	**Preliminary design specifications**
Storage module	• 135-MW$_e$ discharge electric generation capacity • 26-GWh$_{th}$ storage capacity (100 hours at full-load discharge capacity) • Round-trip efficiency >50%
Particles as storage media	• Silica sand with >99% silica purity, stable at >1,200°C • Cost: $30–40/ton
Electric charging particle heater	• 315 MW$_{th}$ • Thermal efficiency ≥98% • Outlet particle temperature ≥1,200°C
Particle thermal energy storage	• 7 GWh$_{th}$ per storage silo • Storage temperature ≥1,200°C • <1% thermal loss per day
Lock Hoppers	• Feeds hot particles from ambient-pressure storage to PFB HX. • A pair of lock hoppers operate alternatively to maintain constant particle flow into PFB HX.
Pressurized fluidized-bed heat exchanger	• Direct air/particle contact PFB HX design • 300 MW$_{th}$, 292 kg/s air flow rate, 300 kg/s particle flow rate • Air inlet temperature = 300°C • Air outlet temperature ≥1,170°C
Air-Brayton combined-cycle power system	• Refractory-insulated piping for air connections • Air-Brayton combined cycle • >52% power generation efficiency

Figure 1 shows the schematic of the particle ETES system in a full-scale configuration with the components specified in Table 1. The particle storage containment was designed to store particles at both heated (1,200°C) and cooled (300°C) conditions and uses a concrete silo with refractory insulation liners. The particle TES uses stable, inexpensive silica sand and provides large storage capacity and high-temperature energy. The silica sand is produced in the U.S. Midwest and has >99% SiO_2 purity, making it stable while operating at high temperatures (>1,200°C) with a low material cost.

Detailed studies have been performed on the thermal stability, material compatibility, and the characterization of physical properties of silica sand. The durability of silica sand has been tested for 500 hours at 1,200°C with the presence of refractory coupon samples. Thermal cycling tests were performed between 300°C and 1,200°C for 100 cycles, and no obvious size change was observed, as shown in Figure 3. These thermal tests verified both the stability and the compatibility of the particles with the refractory insulations [17]. Figure 3 shows typical results from the thermal cycling tests and the heat capacity measurements of a silica sand type 460 supplied from Covia [18]. The thermo-cycle test results shown in Figure 3 indicate size changes of approximately 3% after 100 thermal cycles. The results indicate particles with adequate stability in service life, and fine particles generated from storage cycles can be replenished regularly to maintain a desired particle size distribution inside the system.

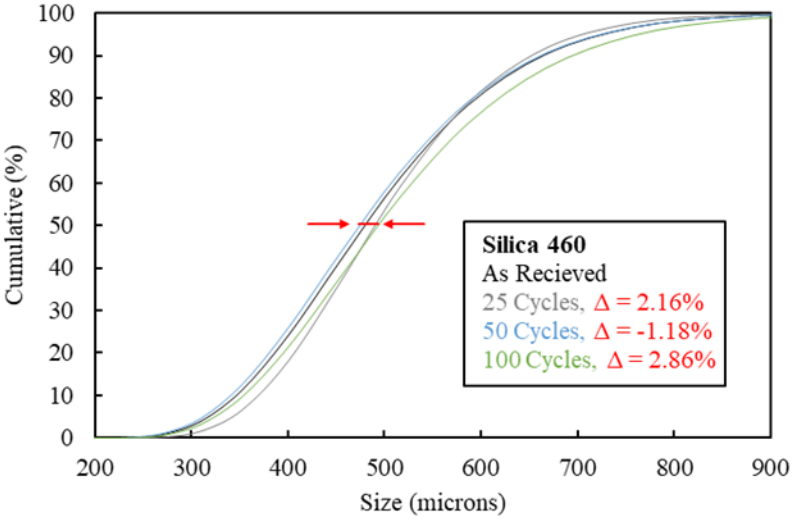

Figure 3. Particle distribution shifts after 25, 50, and 100 cycles relative to the baseline for silica type 460.

Figure 4 shows the specific heat as a function of particle temperature from National Institute of Standards and Technology data sources and actual differential scanning calorimetry (DSC) measurements taken by using a Netzsch STA 449 F3 Jupiter. The heat capacity of silica sand varies with temperature and has a peak point associated with α-β quartz inversion. The negative effects of α-β quartz inversion at approximately 573°C on particle durability or fluidization have not shown up in thermal cycle tests nor PFB prototype tests. The average specific heat capacity within the operational temperature range of 300°–1,200°C is greater than 1.1 kJ/kg-K, indicating an adequate capacity for sensible heat energy storage.

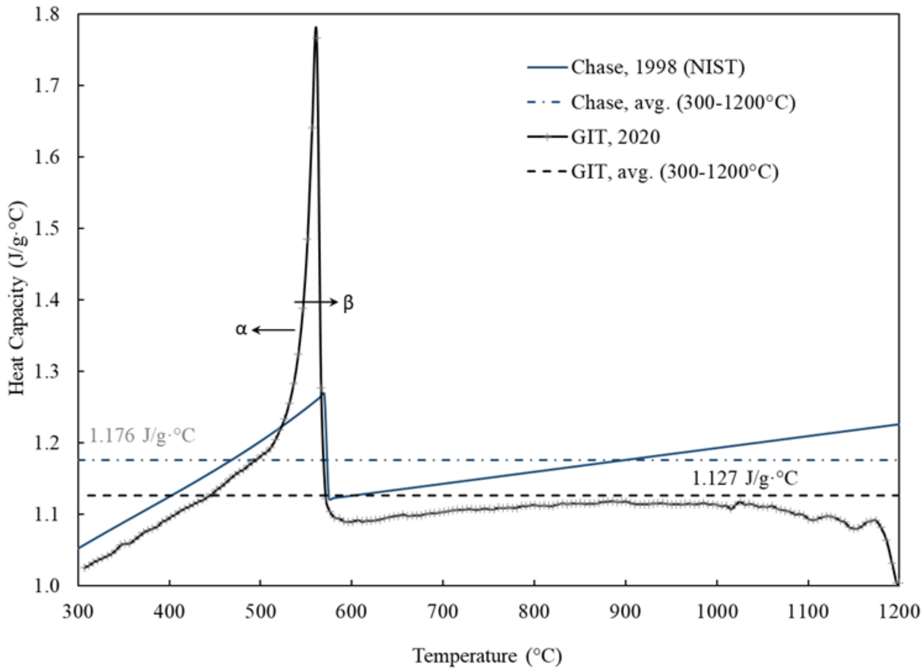

Figure 4. Heat capacity of quartz from 300°C–1,200°C including the α-β inversion at 573°C [16], [18] and specific heat versus temperature measured by DSC (Netzsch STA 449 F3 Jupiter ®).

Silica sand is mined in the Midwest of U.S. and selected from product lines with high SiO2 purity (>99% as shown in Table 2). High silica purity provides stability of particles from sintering or agglomeration at high temperatures. Table 2 summarizes other thermal/physical properties of silica sand. The mined sand maintains desired roundness for flowability, and similar particles have also been used in fracking applications. Vendor quotes indicate silica sand cost of $30–40/ton, which is a fraction of the cost of molten salt or other thermal storage media.

Table 2. Physical properties of the silica sand as storage media

Particle properties	Value	Unit
Particle average diameter	450	μm
Real particle density	2,650	kg/m^3
Bulk particle density	1,543	kg/m^3
Thermal conductivity (bulk)	1.402	W/m-K
Specific heat (temperature dependent)	Figure 4	J/kg-K
Composition [18]		
SiO_2	99.65%	
Al_2O_3	0.065%	
Fe_2O_3	0.018%	
CaO	0.012%	

TiO_2	0.011%

With the verified silica sand as storage media, the system uses insulated concrete silos as TES containment to hold the heated and cooled particles. The TES module is scalable with flexible storage capacity depending on the grid storage needs. The storage capacities can be sized to an electricity discharge duration ranging from less than 10 hours to more than 100 hours. The 100-hour, long-duration storage module shown in Figure 1 consists of four particle containment silos and one buffer silo for temporary transfer of particles. Each containment silo stores both hot and cooled particles, thus eliminating nearly half of the storage containment cost compared to separate hot/cold storage. A buffer silo is used to temporarily store low temperature particles when a containment silo is not completely emptied during discharging, enabling flexible charging/discharging operations. A single full TES silo stores 6.5 GWh_{th}, or approximately 25 hours of full-load, 135-MW_e ABCC operation based on an existing air turbine combined-cycle system as described in Section 3.4. Four TES silos contain approximately 26 GWh_{th} to provide 100-hour storage duration as one storage module. Static stored particles reduce thermal conduction during the storage period by forming a self-insulating layer. With the internally insulated TES containment, heat loss can be limited to less than 1% per day using the insulation designs that were previously analyzed [19].

3. Key Component Development and Prototype Verification

With low-cost silica sand and containment, particle TES represents an economic energy storage method. The particle TES is designed at a high storage temperature (1,200°C) to support a high efficiency thermal-power cycle. Such temperatures present unique challenges for developing and deploying TES and PFB HX components; however, the challenges could be justified because power conversion efficiency is determined by thermal-cycle efficiency, wherein higher particle temperatures allow for a higher turbine inlet temperature to achieve higher thermal-power-conversion efficiencies.

Key components were developed on a conceptual level to address these challenges and to assess the design feasibility, manufacturability, and integration within the system. Table 3 lists key components (except for the ABCC power cycle) along with laboratory prototypes or modeling analysis for verification of the design and operation.

The laboratory prototypes have been built for verifying the component operation and/or validating the modeling methods. The validated models are then used to gauge commercial-scale performance. The conceptual designs, prototype development, and testing validated the component modeling approaches, fabrication processes, and operation mechanisms. The key components listed in Table 3 with the ABCC power generation system are described individually in the subsequent sections.

Table 3. Key component designs and laboratory prototypes for the particle ETES system

Key components	Proof of concept by modeling and/or testing	Design approach, working mechanism, initial performance targets, and relevant industry practices
Heater 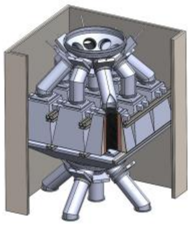	Heater prototype 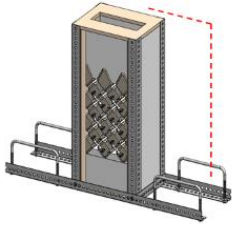	• Heating wires are wrapped around refractory bars form the heating elements to heat particles to 1,200°C using electricity. • Modular design with each module running at a fixed particle flow rate for optimum particle heat transfer and constant power in on/off mode. • Nine heater modules can support nine charging load levels.
Particles/storage 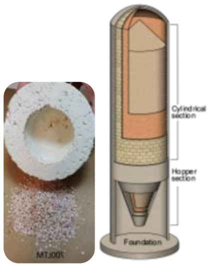	Storage bin prototype 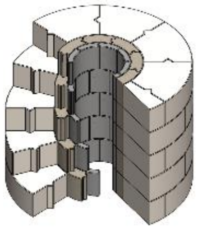	• Low-cost storage using silica sand ($30–$40/ton) with particle stability is verified at 1,200°C. • Charging and discharging temperatures range from 300°C to 1,200°C. • Concrete silo with internal insulation using low-cost refractory materials with conventional construction methods. • Tests proved material compatibility at operating temperature.
Heat exchanger 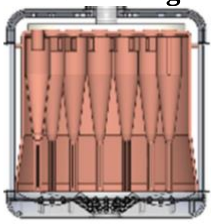	Cold/hot prototypes 	• Direct contact between compressed air and hot particles inside the PFB HX eliminates the heat transfer interfaces in a conventional heat exchanger; thus, it can achieve high temperature without expensive materials for the heat transfer surfaces to improve performance. • Industry PFB HX design, engineering, and fabrication for a PFB boiler can be leveraged.

3.1. Electric Charging Particle Heater

The storage system starts from an electric charging particle heater that is designed and operated in modules. Electric resistive heating is inexpensive and efficient, with a theoretical 100% electric-to-thermal conversion efficiency by resistor heating if the electric heater is perfectly insulated. The heater is designed to be flexible and easily controlled for rapid ramping rates and charging responses. The simplicity in charging particle TES using an electric heater provides implementation convenience in ETES usage for electricity storage.

Stable silica sand is used as a storage media. Silica sand is not corrosive and is compatible with refractory materials, thus providing flexibility in selecting heating element materials, thermal insulation, and element shapes; however, heating particles with an electric heater relies on particle granular flow and heat transfer, which is less effective than heating a liquid media such as water or molten salts. To deal with the challenge of particle heat transfer, modeling and prototype testing were performed to characterize the particle flow and heat transfer. Here we present a preliminary design with an optimized heat transfer process and heating element choice for charging the particle ETES system.

3.1.1 Particle Flow and Heat Transfer Simulations

The electric charging heater is uniquely designed in a modular configuration for particle flow and load control [20]. Figure 5 illustrates the charging heater assembly and heater designs. The heater has arrays of hexagonal-shaped heating elements to heat particles in granular flow. Each heater module is individually internally insulated and supported by an external structure. An individual module operates at a fixed heating capacity with a designated particle flow rate designed for the most effective heat transfer rate, and independent on/off control per module enables stepped control of the overall heater load.

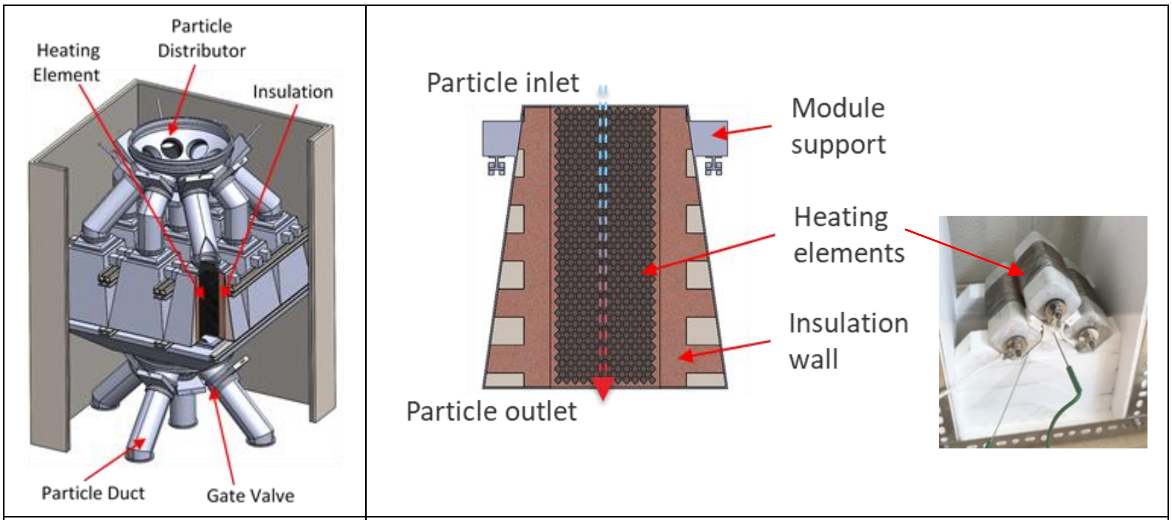

a. Heater assembly

b. Charging heater module and heating elements

Figure 5. Modular design of electric particle heater for charging particle TES (Photo by NREL).

The operation of all nine modules shown in Figure 5.a provides a full charge load, and the operation combinations of modules creates nine load steps. Figure 5.b shows the module design, which consists of arrays of hexagonal-shaped heating elements. Particles fall through the heating elements in a granular flow pattern and are heated to the desired temperature. The particle flow rate is regulated by the shape of the heating elements and the gaps between them. A strong silica-carbide based refractory material with high hardness is used for the heating elements to support metal heating wires and to provide erosion resistance to particle flow.

Particle granular flow simplifies the charging heater design relative to a fluidized bed and improves particle heat transfer relative to a dense, moving packed bed particle flow regime. Particles drop through staggered, hexagonal-shaped heating elements such that periodic mixing and direct contact with the heating surfaces enhance particle heat transfer. The shape, size, and arrangement of the heating elements were optimized to achieve the desired particle flow and heating effectiveness. Improving particle heat transfer increases power density and reduces the size, cost, and heat losses of the heater. Both modeling and testing were performed to investigate particle flow through the heating elements and to realize the desired heat transfer.

3.1.2 Particle Flow and Heat Transfer Simulations

The heater design was initially analyzed by mathematical modeling of particle granular flow around the heating elements. The model was developed using the discrete element method (DEM) in Multiphase Flow with Interphase eXchanges (MFIX) software [21–23]. The modeling methods and simulation parameters are provided in Appendix A.1, which lists the conservation equations, modeling approaches, and input parameters.

The primary parameters of interest are those that influence the rate of heat transfer, including: (1) heating element geometry, angle, and spacing; (2) inlet hopper angle; (3) particle-particle friction; and (4) particle wall friction [24]. Shallow hopper angles are ideal for heat transfer because they increase the particle residence time; however, a small slope angle, θ, increases the risk of particle flow stagnation. Also, increasing friction coefficients dilute the particle flow, which decrease the heat transfer. Those effects were simulated by the MFIX heater model, which guided the heater design and performance analysis. Figure 6 shows the computational domain and results for a few select cases from the parametric study detailed in [24].

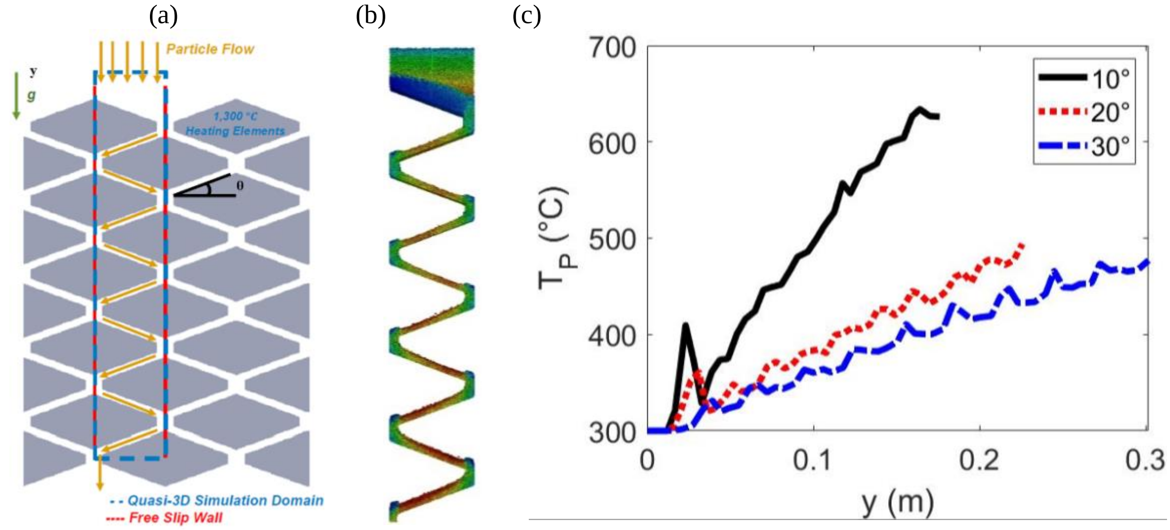

Figure 6. Overview of MFIX-DEM modeling effort, including (a) definition of modeling domain, (b) particle velocity contour plot, and (c) average particle temperature profiles for several geometry angles as a function of heater depth over the computational domain.

In Figure 6.c, all simulations are set to control the particle flow state via the heating element geometry and the gap between elements. Hexagonal-shaped heating elements break down the particle flow stream, provide direct contact for particle heating, and blend particles through each flow path, resulting in a high heat transfer rate for charging hot particles. The particle temperature profile and mass flow rate from the DEM simulations are used to determine the effective heat transfer coefficient, ranging from 500 W/m^2-K–1,500 W/m^2-K, depending on the geometry and friction coefficient. This heat transfer coefficient can then be used to define the heater sizing necessary to achieve the design outlet temperature conditions in a large-scale heater array. Figure 6.c shows the particle temperature along the height of the heater with three slope angles (θ) of the heating elements.

The heater model has been used to extend a section of the modeling results to inform the full-scale design. Particles often develop flow instabilities, as indicated by the unsmooth curves in the temperature profiles in Figure 6.c. The spike at the top of the simulation is due to stagnant particles on the first row of heaters. Stationary particles are not seen in subsequent rows. Figure 6.c indicates that a small slope angle or less steep top of the heating elements improves heat transfer because of the slow flow rate and correspondingly longer heating time associated with a flat heater top; however, a small surface angle risks particle flow stagnation. Thus, flow visualization testing is being applied to observe the particle flow patterns and to select the geometry of the heating elements.

3.1.3 Particle Flow Visualization Test

Experimental particle flow test stations were adapted to mirror the MFIX-DEM modeling domain for various candidate heating element geometries to determine the mass flux at ambient temperature. Figure 7 shows several flow visualizations and the resulting particle mass accumulation rates. In total, four different flow stations were used to test more than 10 heating element arrangements with varied geometries, angles, and spacing. The measured particle mass accumulation rates in Figure 7 indicate steady particle flow rates and therefore good particle flowability for a variety of heating element configurations.

Particle heat transfer rates with the heating elements affect the heater size, thermal efficiency, and cost. The simulations in Section 3.1.2 provide insights for which designs achieve effective heat transfer. Substantial development is ongoing to verify the performance of the heating elements and to validate the heat transfer rates predicted from the DEM simulations. Prototypes have been fabricated using an electric resistive heater with heating wire wrapped on hexagonal-shaped refractory supports (Figure 5.b). Tests will focus on particle flow and heat transfer to validate the heater module design and will be reported in future publications.

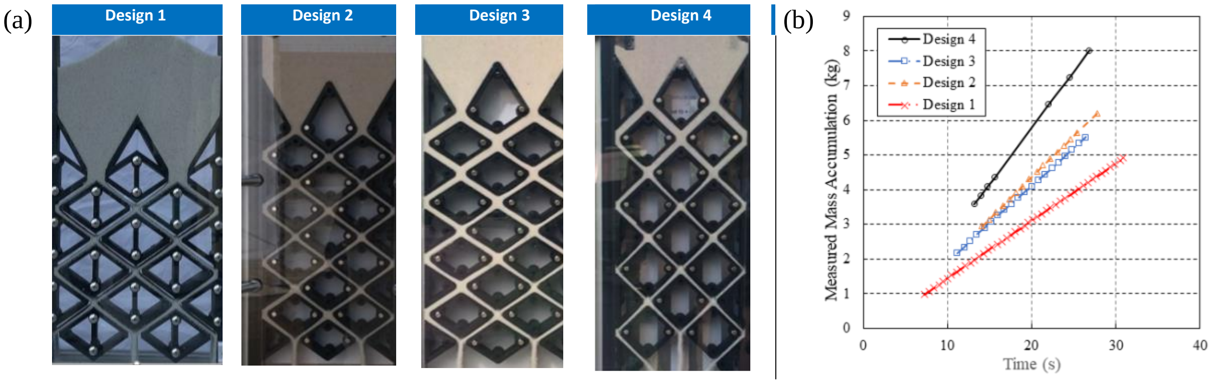

Figure 7. Experimental results including (a) testing of four different cases from the parametric study described in Section 3.1.2 and the (b) determination of the resulting mass flow rates.

3.2. Particle TES Design and Modeling

The high-efficiency particle TES is charged by electric heating, and hot particles are stored in well-insulated containment. The TES containment consists of a concrete silo and refractory insulation to hold hot particles at conditions commeasurable with the material usable temperature and thermal loss target. The design was based on high-thermal-efficiency TES development for a particle-based CSP system and followed codes and standards for concrete structures cited by [25] [26]. Commercial refractory materials and industry experience in refractory installation were considered while designing and performing a cost assessment of the TES containment.

The silo shown in Figure 8 is internally insulated with refractory lining and insulation layers. This is to maintain the temperature of the concrete silo below the concrete allowable use temperatures. The TES capacity, size, and cost were estimated using material data and earlier particle TES design work, adjusted by high energy density in the LDES system due to a larger temperature difference. Using silica sand provides higher particle density and higher heat capacity than the coal ash described in our original work [26]. Storing large volumes of granular media in silos is well established in industry; however, heating and storing ultrahigh temperature particles while minimizing heat loss requires an innovative design. Applying insulation inside a tall silo can be challenging and was evaluated by our industry partner specializing in refractory materials. Large refractory blocks can be fabricated and stacked inside the silo to form a modular insulation layer.

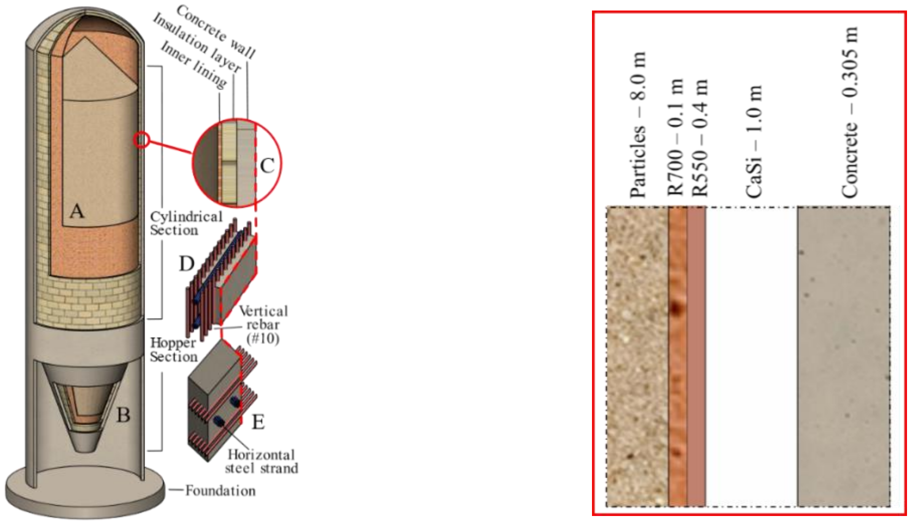

a. TES containment design for particle storage

b. Zoom-in Section C: TES insulation materials and dimensions

Figure 8. Particle TES containment design and insulation layers.

Figure 8.a shows the containment structure, including concrete silo and insulation layers. Section views “A” and “B” show the cylindrical and hopper section contents, respectively. Detail “C” shows the wall configuration, which comprises an inner lining with strong refractory (R700) for erosion resistance, insulation layers, and outer concrete wall, as illustrated in Figure 8.b. “D” and “E” renderings show the rebar and strand layouts within the concrete walls of the cylindrical and hopper sections, respectively. Figure 8.b shows the TES insulation material selection and layer thickness for the performance results described next.

To reduce the overall containment cost, both hot and cold particles are stored in the same well-insulated silo in a thermocline configuration. The development of the low-cost particle TES was reported previously for a 100-MW_e steam Rankine power cycle with a TES capacity of 6.5 GWh_{th} per single silo and 26 GWh_{th} with four silos for a 100-hour duration [27]. Storing both hot and cold particles in the same silo with stratified layers can reduce the containment cost by nearly half. During discharge, hot particles feed into the PFB HX by gravity and heat the fluidizing air, which is then used to drive the turbine to generate electricity. An industrial particle conveyor is used to transport the cold particles from either the particle exits of the PFB HX to the top of the silo (during discharging) or from the outlet of the silo to the particle heater (during charging). The electricity storage cost depends on the thermal-power conversion efficiency. The estimated TES cost including storage media, concrete silos, and insulation was estimated to be approximately \$2/kWh_{th} [27]. For a 50% round-trip efficiency, a simple conversion implies an electricity storage cost of approximately \$4/kWh_e for the storage media and containment, not including the capital cost of power generation. The cost of energy storage media and containment can be an order of magnitude lower than most storage methods [4]. Recent developments have further assessed the economics of particle TES and support its potentials in LDES [10] and industry process heat.

Minimizing thermal loss rates through the TES containment is critical to maintaining high particle temperatures, and thereby high thermal-to-electric efficiency during discharge, for long-duration storage applications. Transient finite element analysis (FEA) models were developed for both prototype-scale and commercial-scale TES containment analysis. Appendix A.2 shows the thermal models using the FEA method and applies different operating conditions and geometries appropriate to each scale.

To study the tradeoff between insulation design, system performance and cost, a transient, 1D thermal insulation model. Figure 9 shows the thermal resistance model with various insulation layers, concrete walls, and ambient heat transfer as well as defines key variables such thermal resistance, energy flows, material properties, and dimensions. Three insulation mechanisms are analyzed between the bulk particles of the storage silo and ambient environment. First, a film layer comprised of two parallel resistances represents the film conduction of the gas *g* and particle *p* phases. This film layer is considered mass-less with no thermal mass. Second, the primary insulation layers are designed with four insulation layers as shown in Figure 8.b**Error! Reference source not found.**.

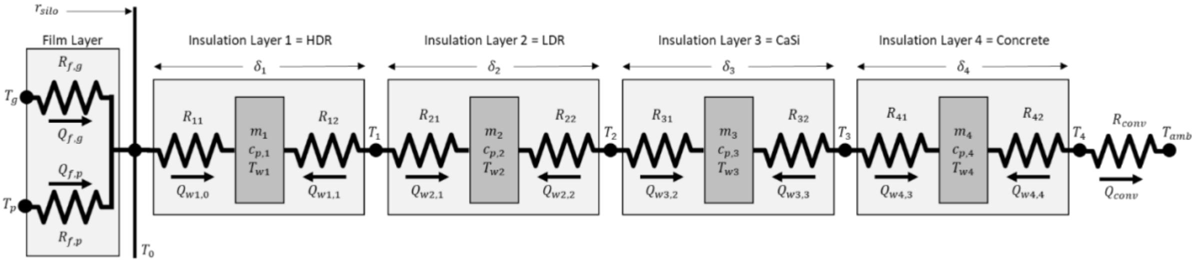

Figure 9. Graphical representation of the mathematical description of both the volume and insulation model that comprise a single particle storage silo model.

Four layers have significant mass and heat capacities such that they absorb, store, and release thermal energy. Insulation layer *j* is assumed to have a mean temperature at the center of the given insulation layer T_{lj}. Lastly, there is the convective thermal resistance R_{conv} between the exterior wall of the particle storage silo and ambient. Gas and particle temperatures, T_g and T_p, respectively, are the connection points between the insulation and thermal mass sub-components of the overall particle storage model. Ambient temperature T_{amb} is considered a fixed parameter. T_g, T_p, and T_{amb} are the boundary conditions for the insulation model. The film layer thermal resistances are defined as follows:

$$R_{f,g} = \frac{\delta_{f,g}}{\pi D_{silo} H_g k_g} \tag{1}$$

$$R_{f,p} = \frac{\delta_{f,p}}{\pi D_{silo} H_p k_p} \tag{2}$$

Where H_g and H_p are the height of the gas and particle medium in the storage silo at a given time, respectively, $\delta_{f,g}$ and $\delta_{p,g}$ are the gas and particle medium film thickness, respectively, and D_{silo} is the inner diameter of the silo. The thermal resistance between node i and layer j is as follows:

$$R_{i,lj} = \frac{\ln\left[\dfrac{r_{silo} + \sum_{j=1}^{j-1}\delta_j + \frac{1}{2}[2-(j-i)]\delta_j}{r_{silo} + \sum_{j=1}^{j-1}\delta_j + \frac{1}{2}[1-(j-i)]\delta_j}\right]}{2\pi H_{silo} k_j} \quad \forall j \in J, i \in \{j-1, j\} \tag{3}$$

Each insulation layer has two thermal resistance terms: one for the inner half of the cylindrical layer and one for the outer half of the cylindrical layer. The thermal resistance model was used to study insulation performance and its sensitivity to design and cost.

The simple transient, 1D heat equation model was built to first screen potential insulation designs (i.e., thicknesses of each layer). The model used a standard commercial partial differential equation solver. This preliminary sizing tool saved using the significantly more computationally expensive FEA methodology to iterate over the insulation design.

The simple thermal model yielded a promising insulation design that was in line with thermal limits of materials. The insulation design is shown in Figure 8.b. This insulation design was applied to a commercial-scale particle storage silo geometry. The commercial-scale model examines a storage silo designed to store 6.5 GWh_{th}. A FEA model used the simulation software (ANSYS Mechanical), solution methodology (Appendix A.2), and refractory materials as the prototype-scale model and experimental setup. The FEA model solved the 3D, transient heat equations as detailed in Appendix A.2. The results of the commercial-scale FEA model are shown in Figure 10.

The computational results show that the insulation design retains 98% of the thermal energy after 5 days of storage, with an average particle temperature greater than 1,180°C as shown in Figure 10.a. This high efficiency of the storage silo was relatively insensitive to ambient conditions and operating cycles. The one-dimensional temperature profile in Figure 10.b shows the radial temperature distribution through the particle domain and the various insulation layers. Particles within the 7-m radius core remain very close to 1,200°C even after 5 days of storage. This illustrates the self-insulating effects of the particles due to their solid, static nature (compared to a liquid storage medium in which free convection can induce mixing).

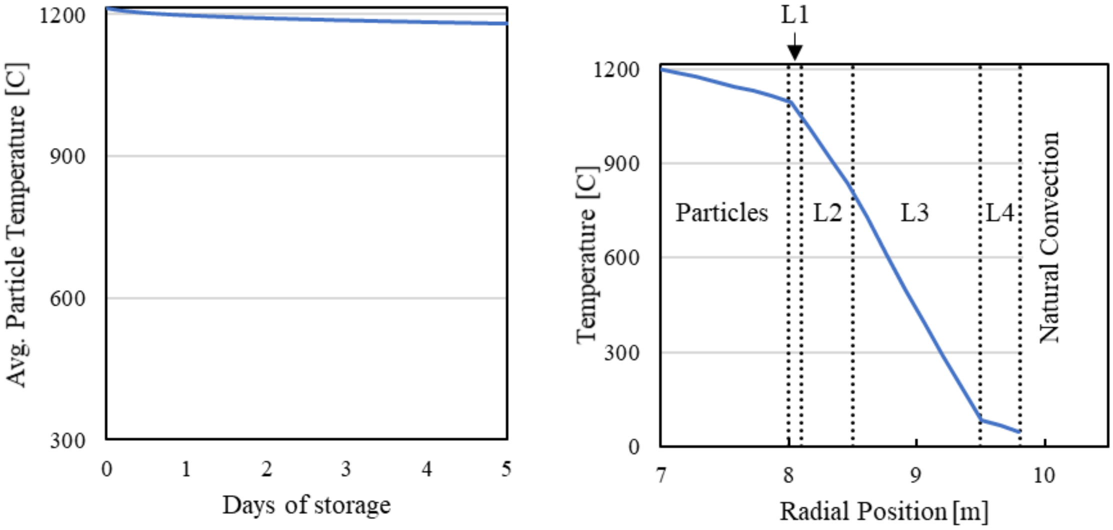

a. Average particle temperature over 5 days (120 hours) of storage

b. Radial temperature profile after 5 days of storage

Figure 10. Temperature profiles from product-scale TES containment model.

Layers shown in the temperature profile in Figure 10.b include L1: high-density refractory lining, L2: low-density refractory layer, L3: calcium silicate, and L4: concrete. The temperatures through insulation layers L2, L3, and L4 drop substantially, and they are lower than 100°C on the inner face of the concrete silo, which ensures that the concrete structure is within its thermal allowance. The insulation design simulated here achieved the target <1% energy losses per day.

3.3. Discharge Heat Exchanger

Conventional heat exchangers use a heat transfer interface separating the two heat transfer media, such as shell-tube or plate-plate heat exchangers. Heat exchanger designs for hot particles with a working fluid often take on one of two types of configurations: a moving packed bed or a fluidized bed. The PFB HX is a unique design that provides direct heat transfer between the hot particles and pressurized air [10]. The uniqueness of the PFB HX is the air/particle direct contact counterflow heat transfer in the commercial-scale design. The outer shell holds pressure, whereas an inner shell contains the high temperature counterflow PFB HX. The airflow is directly integrated with the compressor and turbine through a tube-in-tube connection. The direct air/particle contact eliminates the heat transfer surfaces, thus eliminating the interface materials and their associated temperature limitations and cost.

Figure 11.a illustrates the design of a PFB bed for direct air/particle heat transfer. The commercial-scale PFB HX design was derived from a PFB combustion boiler after removing coal combustion and pollution reduction systems [28]. The PFB HX design is configured to directly heat pressurized air by hot particles in a counterflow fluidized bed. Cold pressurized air from the compressor of the turbomachinery flows through the fluidized bed. In an ideal case, air exits the PFB HX at the hot particle temperature to drive the downstream turbomachinery to produce power. Aspects of the PFB HX and ABCC loop were derived from a commercial PFB boiler integrated with a GTCC system [16,28].

Figure 11.b shows prototype test stations for cold and hot prototype testing, respectively. The cold prototype test is for observing fluidization conditions using a transparent vessel. The hot prototype was developed to investigate the air/particle heat transfer performance and operation of the PFB HX at design conditions of approximately 1 MPa and at an air exit temperature of 1,170°C.

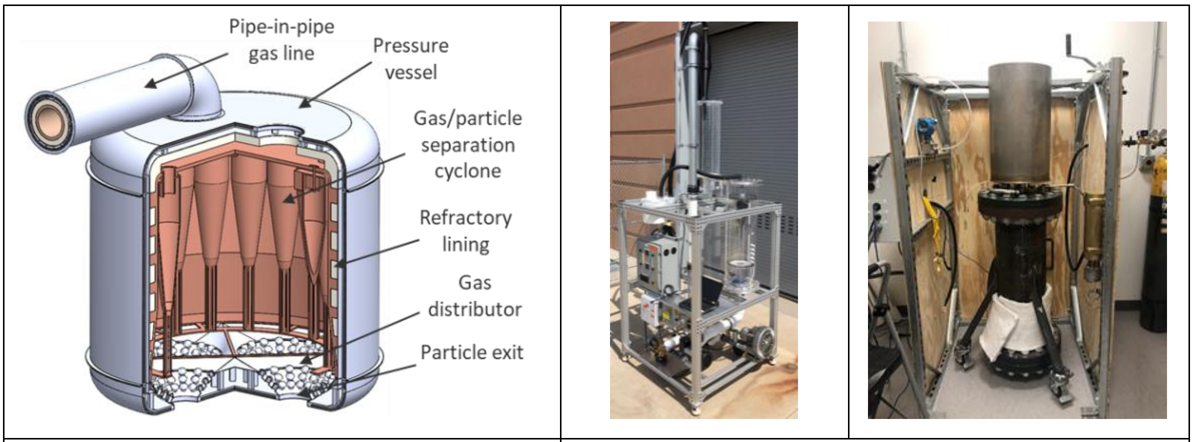

a. Commercial-scale PFB HX conceptual design

b. Cold (left) and hot (right) prototype testing stations

Figure 11. The design of a PFB for direct air/particle heat transfer (images by NREL and Purdue).

Figure 12 shows the cold prototype PFB bed and test results by measuring the airflow and pressure drop at ambient temperature and pressurized condition up to 250 kPa. The cold prototype uses transparent plastic columns for flow visualization. It verifies the fluidization condition and minimum fluidization velocity through pressure measurement and direct observation.

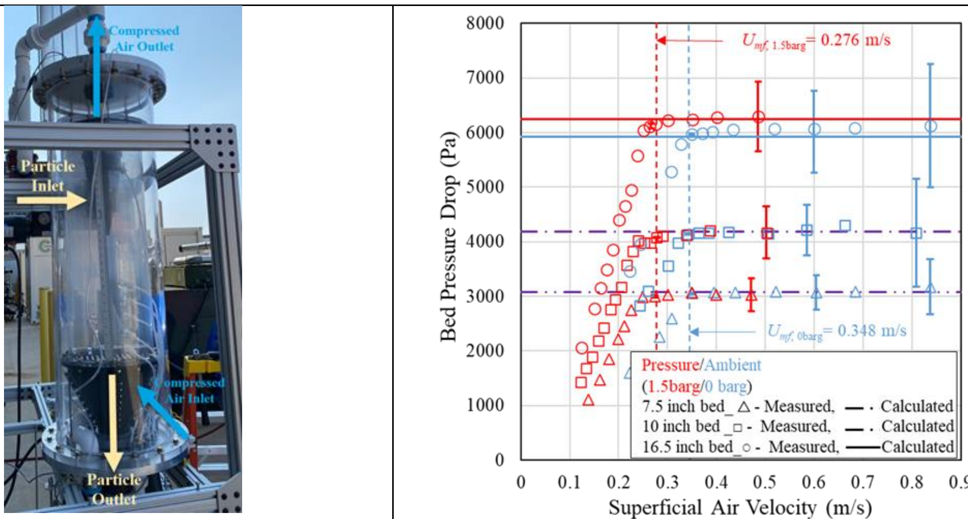

a. PFB prototype for fluidization test at ambient condition (Photo by NREL)

b. Test results of fluidization conditions and pressure drop

Figure 12. Cold PFB prototype fluidization test at ambient, pressurized conditions (250 kPa).

Minimum fluidization occurs when the bed pressure becomes constant with increasing air velocity, indicating that the fluidizing air suspends the particle weight. The minimum fluidization velocity for an initial bed height of 0.191 m (7.5 in.), 0.254 m (10 in.), and 0.419 m (16.5 in.) was measured to be 0.276 m/s on average at ambient temperature and an absolute pressure of 250 kPa. Figure 12.b indicates good agreement between the measured pressure drop and the theoretically calculated pressure drop and shows a consistent minimum fluidization velocity across bed heights.

Hot prototype test results are shown in Figure 13.b. Temperature measurements are shown at two locations within the fluidized bed, denoted as “Sand Top” and “Sand Bot” in the legend, alongside the heater set point temperature and air temperature above the fluidized bed. Figure 13.b indicates that the internal fluidized bed can reach high temperatures while maintaining relatively low temperatures in the surrounding pressure vessel (denoted as “PV”).

Based on the prototype for testing, prototype-scale and product-scale models of the PFB HX have been developed by using Computational Fluid Dynamic (CFD) software ANSYS/Fluent. The aim is to use the prototype-scale model to validate the CFD methodology and framework against the prototype testing results shown in Figure 13. Then the validated approach will be applied to the study of the commercial-scale performance of the PFB HX. The Eulerian-Lagrangian DEM approach is feasible for the prototype scale but is intractable for a commercial-scale PFB HX. The CFD models use a Eulerian-Eulerian (two-fluid) method to reduce computational expense compared to a Eulerian-Lagrangian approach. Mathematical method of Eulerian-Eulerian two-fluid model is described in Appendix A.3. Both prototype-scale and commercial-scale models operate at on-design, commercial conditions (P = 1 MPa, T = 1,200°C). The prototype-scale model matches the geometry of the hot prototype test, whereas the commercial-scale model matches the geometry of a conceptual 300-MW_{th} PFB HX.

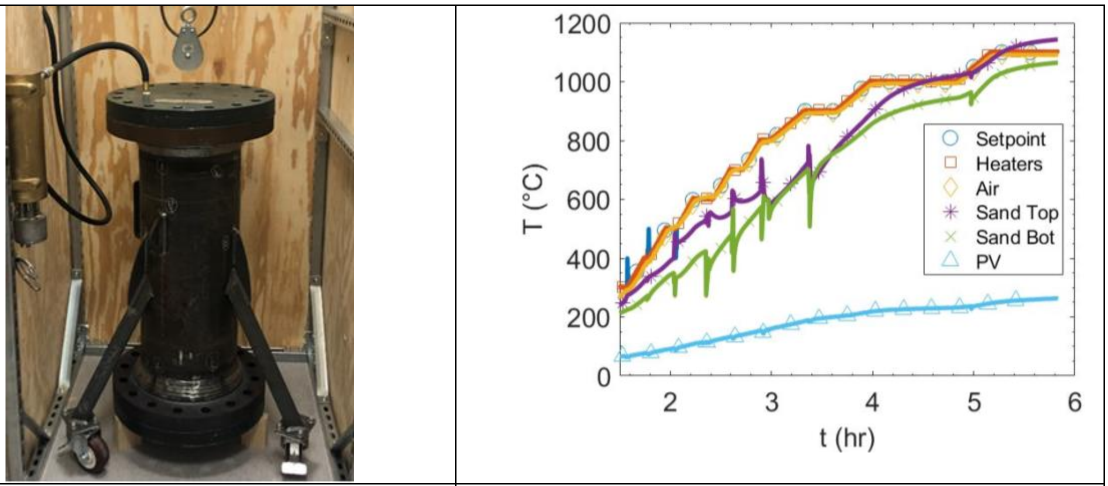

a. Hot PFB prototype for air/particle heat transfer and fluidization

b. Hot prototype test results of air heated by hot particles

Figure 13. The design of a PFB for direct air/particle heat transfer.

Figure 14 shows a sample result from the CFD models of a product-scale PFB HX. Figure 14.a shows how effectively the inlet air is heated from an initial temperature (300°C) to the bed temperature (1,200°C). In both cases, the air temperature exceeds 1,180°C. The relatively flat temperature profile through the bed region (the shaded grey area) is consistent with the high particle surface area and correspondingly high particle-to-air heat transfer surface area.

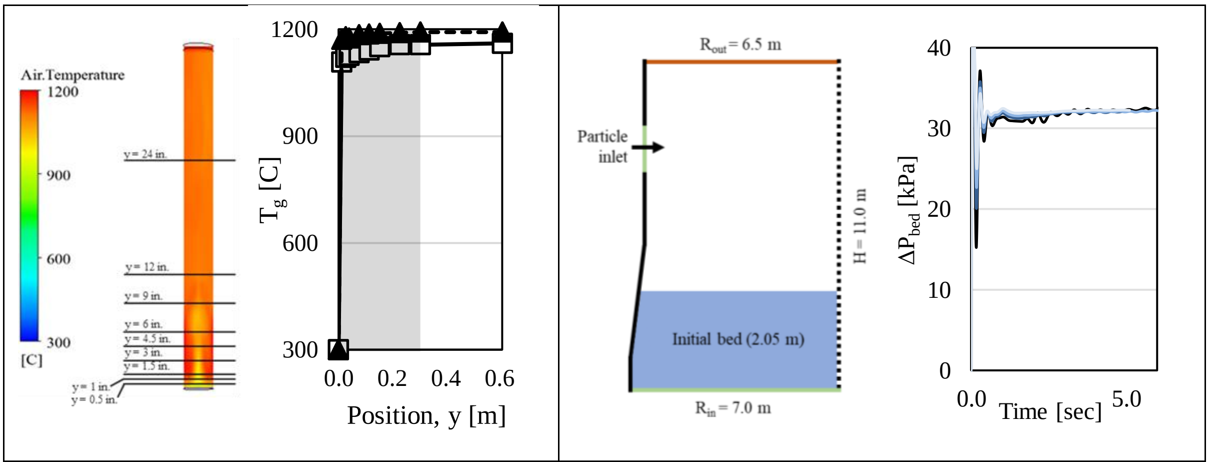

a. Prototype-scale temperature profile

b. Commercial-scale transient bed pressure drop

Figure 14. Sample results from both scales of CFD models of PFB HX.

Figure 14.b shows the transient air pressure drop across the bed at startup conditions for the commercial-scale PFB HX. Initial transient spikes in bed pressure drop dissipate in less than 5 seconds and stabilize in normal PFB HX bed operation. Any additional fluctuations are minor and are associated with small bubbles continuing to rise through the bed. The steady-state bed pressure drop is approximately 34 kPa (or less than 4% of the turbine inlet pressure). Some additional pressure drop would occur across the air distributor, cyclone separator array, and piping.

The heated exit air from the PFB HX then flows through an array of air/particle separation cyclones inside the pressure vessel to remove the entrained particles from the airstream. Air/particle cyclones are proved devices in cleaning particles from air stream with broad industry uses and household vacuum machines for dust removal. They can be very effective to remove fine particles from air flow with well-established design practices [29]. Cyclones were successfully used in fluidized bed boilers in connection with gas turbines [30]. The cycle design in this PFB HX used the design method in [29] and achieved particle separation cutoff size of <10 µm in particle diameter at 2.8 kPa pressure drop, which meet the turbine and system performance requirements set up by the ABCC integration.

Preliminary results from the commercial-scale PFB HX model indicate that the commercial-scale PFB HX will have the same high heat transfer effectiveness as the prototype-scale PFB HX. These CFD models will be further validated using prototype testing results and will serve as design tools to examine on- and off-design performance, future design decisions (e.g., distributor design, internal baffling), ramp rates, and performance at different operating conditions of a commercial-scale PFB HX for particle TES applications.

3.4 ABCC Power Generation Integration

The PFB HX is connected to the power system through a tube-in-tube air connection. Inside the connections, low-temperature inlet air from the turbine compressor flows in the outer shell and maintains a low temperature of the metal shell. Then the heated air flows through the inner pipe, which is insulated by a refractory lining that reduces heat transfer between the hot and cold airstreams. The hot air exits the inner pipe and enters the power turbine section that drives the power generation. Last, the exhaust air exits the turbine, drives a bottom steam Rankine cycle, and is released to ambient at a low temperature.

Pressure losses of the compressed air through the flow path and PFB HX are key to the storage efficiency and power cycle performance. The component design and modeling determined the component sizing iteratively and assessed tradeoffs in the cost and performance to meet targeted pressure losses through each component. Figure 15.a lists the major pressure drops through key components at a design point of 270 MWt/135MWe power generation capacity. Figure 15.b shows the distribution of pressure losses among the flow paths. About 80% of pressure loss occurs in PFB HX, which is primarily caused by fluidizing solid particles and follows calculation by the Ergun equation. The total pressure loss of 42.08kPa is lower than the pressure loss target set in ABCC cycle modeling for >52% cycle efficiency.

a.

Pressure Losses	kPa
Outer Pipe	1.73
PFB Vessel	0.05
Air Distributor	2.5
PFB HX	33.76
Cyclone	2.8
Inner Pipe	1.23
Total	42.08

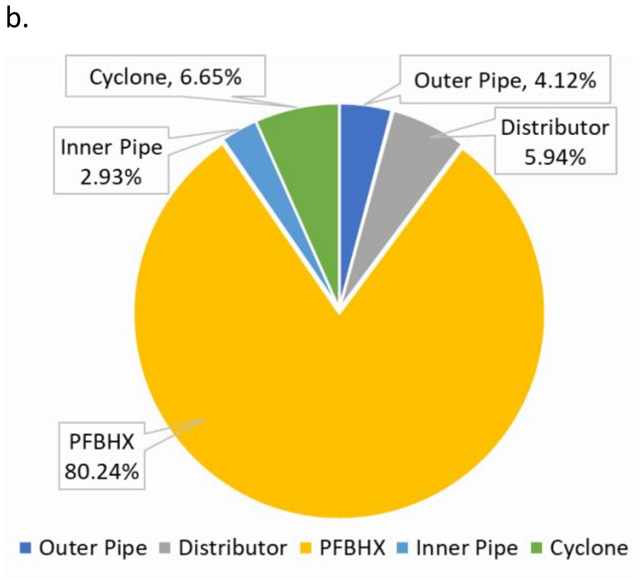

Figure 15. Pressure losses through the flow path and PFB HX to meet the performance requirements.

The direct particle-gas contact is technically necessary and economically feasible to heat the compressed gas using hot particles. The designed exiting temperature of nearly 1200°C prohibits using any metal or metal alloy to contain high pressure gas. The unique PFB HX design enables rapid heat transfer between gas and hot particles and drives the air turbine in the ABCC power system.

The cost and performance of the power generation subsystem are critical to the LCOS of the particle ETES system. Using high-efficiency power cycles is key for high round-trip cycle efficiency. The ABCC power island in the particle ETES system is based on a commercial GTCC product line, which provides low risk and short development time relative to a new power system. The thermal power efficiency of an ABCC power system is largely governed by the turbine inlet temperature. Figure 16 shows the relationship between the turbine inlet temperature and the discharging efficiency [31].

Figure 16 indicates that the turbine inlet temperature (TIT) of the TES system needs to be greater than 1,170°C to reach the 52% cycle efficiency target. A power cycle performance model was developed based on Aspen-HYSYS software. The power system model simulated a Class-E combined-cycle power block by General Electric Global Research to configure the power generation system for the >52% ABCC performance. The cycle model obtained the state conditions of air and particle flow rates, air pressure and temperatures to size the storage components. The cycle consists of a compressor, particle heat exchanger, power turbine, heat recovery steam generator (HRSG), and a steam turbine. Cycle configurations in Figure 2 were considered in both open and closed loops, whereas an open-loop configuration was selected as a simpler system.

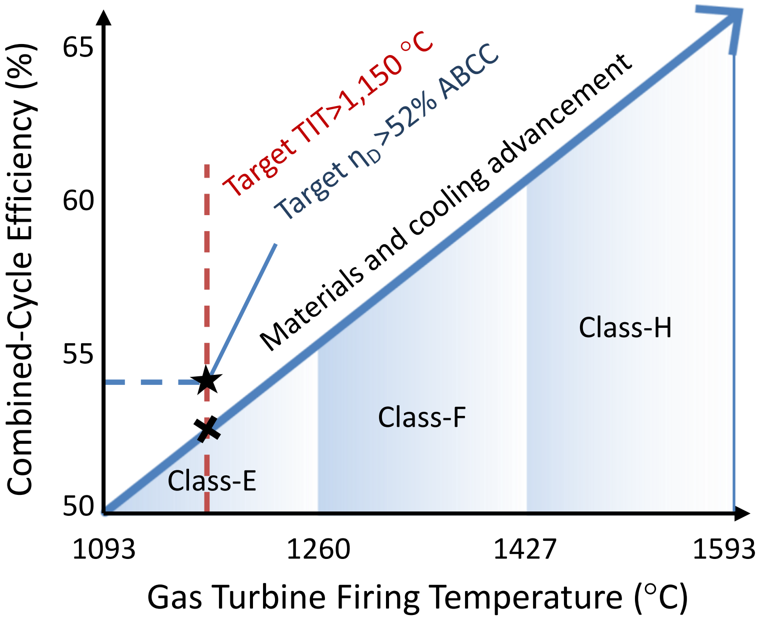

Figure 16. At >1,150°C turbine inlet temperature, the Class-E GTCC can achieve >52% efficiency, and a Class-E turbine was refereed for ABCC performance (Adapted from reference [32]).

The particle TES system can support any thermal-power conversion cycle. ABCC provides a unique opportunity to use existing GTCC product lines without using fuels or developing new turbomachinery. ABCC provides a larger storage temperature range than other power cycles, thus increasing the TES energy density due to a large temperature difference between the hot and cooled storage media. It can also be built upon a retired thermal power plant with an existing steam Rankine or a gas turbine combined-cycle power system to reduce capital investment; however, an emerging pumped thermal energy storage technology offers potential for even higher round-trip storage efficiencies [13,33–36]. Pumped thermal energy storage can increase efficiency for a given turbine inlet temperature by using a heat pump for charging, thereby making it an attractive next-generation ETES technology [35].

Conclusions

A novel stand-alone particle ETES system and associated components were developed for electric energy storage by storing low-value, off-peak electricity in thermal energy, which can then be dispatched as high-value, peak-demand electricity. The particle ETES system uses stable, low-cost particles as storage media and a high operating temperature to drive a ABCC with a high thermal efficiency to meet LDES capacity and economic targets. The system charges storage by directly heating particles with a resistance heater that uses particle granular flow through arrays of heating elements. The heated particles are stored in insulated concrete silos and discharged through a PFB HX. The process and results of modeling, designing, and prototype testing provide component design approaches and operations of key components including electric charging particle heater, pressurized fluidized bed heat exchanger, and particle TES. The heat exchanger using air-particle direct contact for heat transfer between particles and pressurized air reduces its cost by avoiding a heat transfer interface between fluidizing air and particles and can operate at very high temperatures with refractory insulated walls. The direct-contact heat exchanger increases power cycle efficiency by retaining heat and operating at higher temperatures.

The component development and prototype studies indicate the technical feasibility of the particle ETES system for ETES applications. Modeling and initial prototype testing has determined operating parameters that will guide the design and size of commercial-scale components. This study indicates that the performance targets for the particle ETES system, including a round-trip electrical storage efficiency exceeding 50%, are technically feasible. The relatively low cost and high efficiency of particle ETES allows LDES to become a viable and economic means to support renewable integration and maintain electric grid resilience. The large capacity and site flexibility of the particle ETES system has significant potential to complement alternative energy storage technologies, such as battery and PSH, for grid-scale energy storage.

Appendix. Details of Mathematical Models

A.1 MFIX Discrete Element Modeling for Particle Flow and Heat Transfer in Electric Heater

Discrete Element Modeling (DEM) is a precise way to model particle flow and heat transfer. The high precision of the method is inherent because all particles within granular media are tracked. In DEM, the particles are modeled as spheres and their locations are solved with Newton's laws of motion. The surrounding air is modeled as a continuum media and is coupled with the particles. The interactions between the continuum and individual particles are expressed in interaction exchange coefficients, such as interphase drag and heat transfer. Particle-particle interactions are also directly simulated, making this approach more fundamental than the continuum approach because the solid stresses and heat transfer processes do not rely on closures from theory and are a direct output from the forces experienced by individual particles. Table A.1.1 shows the DEM model in MFIX software that solves large number of particles to analyze particle flow and heat transfer inside the heater [22,23,37,38].

Table A.1.1. Governing equations for the MFIX simulations.

Continuum		
Gas Continuity	$\frac{\partial}{\partial t}(\varepsilon_g\rho_g) + \frac{\partial}{\partial x_i}(\varepsilon_g\rho_g u_{g,i}) = 0$	(A.1.1)
Gas Momentum	$\frac{\partial}{\partial t}(\varepsilon_g\rho_g u_{g,i}) + \frac{\partial}{\partial x_j}(\varepsilon_g\rho_g u_{g,j}u_{g,i}) = \frac{\partial}{\partial x_j}(-p_g\delta_{ij} + \tau_{g,i,j}) - I_{gp,i} + \varepsilon_g\rho_g g_i$	(A.1.2)
Gas Energy Balance	$\varepsilon_g\rho_g C_{pg}\left(\frac{\partial T_g}{\partial t} + u_{g,j}\frac{\partial T_g}{\partial x_j}\right) = -\frac{\partial}{\partial x_i}\left(-\kappa_g\frac{\partial T_g}{\partial x_i}\right) + \gamma_{cp}(T_g - T_p)$	(A.1.3)
DEM Particle Flow Model		
Particle position	$\frac{d\boldsymbol{X}^{(i)}}{dt} = \boldsymbol{V}^{(i)}$	(A.1.4)
Linear velocity	$m_p^{(i)}\frac{d\boldsymbol{V}^{(i)}}{dt} = m_p^{(i)}\boldsymbol{g} + \boldsymbol{F}_{nc}^{(i)} + \boldsymbol{F}_c^{(i)}$	(A.1.5)
Interphase Equations		
Gas-Solid Momentum Transfer	$\boldsymbol{I}_{gp} = \frac{1}{\tilde{V}_{CV}}(\boldsymbol{F}_{nc}K_{CV})$	(A.1.6)
Drag Model[27]	$\beta_{gp} = \frac{3\varepsilon_p\varepsilon_g\rho_g}{4V_{rp}^2 d_p}\left(0.63 + 4.8\sqrt{\frac{V_{rs}}{Re_p}}\right)^2 \lvert\boldsymbol{V}_g - \boldsymbol{V}_p\rvert$	(A.1.7)
	$V_{rp} = 0.5\left(A - 0.06Re_p + \sqrt{(0.06Re_p)^2 + 0.12Re_p(2B - A) + A^2}\right)$	(A.1.8)
	$Re_p = \frac{D_p\lvert\boldsymbol{V}_g\rvert\rho_g}{\mu_g}$	(A.1.9)
	$A = \varepsilon_g^{4.14}$	(A.1.10)

	$B = \begin{cases} 0.8\varepsilon_g^{1.28} \; for \; \varepsilon_g \leq 0.85 \\ \varepsilon_g^{2.65} \quad for \; \varepsilon_g > 0.85 \end{cases}$	(A.1.11)
Heat Transfer[29]	$\gamma_{cp} = \frac{6\kappa_g \varepsilon_p Nu_p}{D_p^2}$	(A.1.12)
	$Nu_p = \left(7 - 10\varepsilon_g + 5\varepsilon_g^2\right)\left(1 + 0.7Re_p^{0.2}Pr^{\frac{1}{3}}\right) + \left(1.33 - 2.4\varepsilon_g + 1.2\varepsilon_g^2\right)Re_p^{0.7}Pr^{1/3}$	(A.1.13)

The particle collisions are resolved by the linear-spring dashpot (LSD) model. LSD modeling assumes the particles and walls are soft and compress. The compression is defined like a damped-spring system, hence the name. The spring constants are user-defined and the damping factors are dependent on the coefficient of restitution. The Syamlal-O'Brien drag model [39] is used for the interphase momentum coupling. The particles are frictional based on the simple coulomb friction coefficient model. The coefficient was specified for both the particles and the walls. All relevant constants and parameters associated with the models used are given in Table A.1.2.

Table A.1.2. Assumed properties for the particles, air, and walls used in the DEM simulations

Particle Properties			
Particle diameter	450 µm	Fluid lens radius	270 µm
Particle density	2600 kg/m^3	Coefficient of restitution	0.9
Thermal conductivity	1.402 W/m-K	Young's modulus (for heat transfer correction)	70 GPa
Normal spring constant	100 N/m	Poisson's ratio (for heat transfer correction)	0.17
Tangential spring coefficient	0.286	Minimum conduction distance	27.5, 1000 nm
Normal-to-tangential damping ratio	0.5	Particle-particle friction coefficient	0, 0.15, 0.30
Specific heat	795 J/kg-K		
Air Properties			
Specific heat	1004.2 J/kg-K	Molecular weight	28.7 g/mol
Wall Properties			
Particle-wall friction coefficient	0, 0.15, 0.30	Young's modulus	70 GPa
Poisson's ratio	0.17		

A.2. Insulation Thermal Model

Transient thermal Finite Element Analysis (FEA) method was used to analyze the thermal performance of the storage components of the energy storage system using actual geometries of the components. The mathematical description of the FEA methodology used is presented here.

The governing energy balance equation for a three-dimensional transient thermal FEA analysis is as follows:

$$\kappa(\boldsymbol{X})\nabla^2 T(\boldsymbol{X},t) = \rho(\boldsymbol{X})c_p(\boldsymbol{X},T)\frac{\partial T(\boldsymbol{X},t)}{\partial t} \tag{A.2.1}$$

Thermal conductivity κ, density ρ, and heat capacity c_p are all functions of position to account for changes in materials throughout the domain. Thermal conductivity and density are both assumed to be isothermal for all materials. Heat capacity is assumed isothermal for all materials except for the particle medium. The heat capacity as a function of temperature for the particle medium is shown in

Figure 4. The discontinuity of the particle heat capacity is caused by a change in the crystalline structure of the silica sand at 573 °C. Two linear equations and their associated temperature ranges were incorporated into the FEA model.

To solve the governing equation, boundary conditions and boundary conditions are required. Where possible, FEA models include symmetrical boundary conditions. Convective boundary conditions were applied to all exterior facing surfaces. The value of the convective heat transfer coefficient was calculated based on established natural convection correlations – see Eq. (A.2.2)-(A.2.4). There was a natural convection for upward-facing horizontal faces, downward-facing horizontal faces, and vertical faces; the coefficients C_k and n_k changed depending on the orientation of the surface – see Table A.2.1.

$$Ra = \frac{g\psi(T_k - T_{amb})L_k^3}{\mu_v^2}Pr \tag{A.2.2}$$

$$Nu_k = \frac{h_k\delta}{\kappa} = C_k Ra^{n_k} \tag{A.2.3}$$

$$h_k = \frac{\kappa C_k Ra^{n_k}}{\delta} \tag{A.2.4}$$

where the volume expansion coefficient $\psi = \frac{2}{T_k + T_{amb}}$.

Table A.2.1. Natural convection heat transfer coefficient parameters.

Exterior surface (k)	C_k	n_k
Upward-facing horizontal	0.15	1/3
Vertical	0.10	1/3
Downward-facing horizontal	0.27	1/4

The material properties for the various materials used for all FEA modeling present in this paper are shown in Table A.2.2. Particle properties are assumed to be those of a packed bad or "bulk" properties shown in Table 2, since in all FEA studies the particles are stagnant. The refractory materials and INSL2025 properties come directly from a material supplier. All other material properties are from common, available, and generic materials.

Table A.2.2. Particle TES material properties.

Material	**Thermal Conductivity [W/m-K]**	**Density [kg/m^3]**	**Specific heat [J/kg-K]**
Refractory materials			
Petromax® 700 (P700 / Refractory A)	0.30	1000	1000
Petromax® 550 (P550 / Refractory B)	0.25	950	1000
Lightweight insulations			
Calcium Silicate (*CaSi*)	0.15	288	1030
INSL2025	0.23	400	1140
Mineral wool	0.08	10	837
Structural materials			
Concrete	0.80	2400	750
Steel	60.5	7850	434

A.3 Computational Fluid Dynamics Modeling of Fluidized Bed Heat Exchanger

A Eulerian-Eulerian (E-E) or Two-Fluid Method (TFM) approach was used for the CFD modeling of the fluidized bed heat exchanger. E-E approaches describe the gas and particle as interpenetrating, continuous media as opposed to the DEM approach described above which tracks the discrete particles. The E-E approach is less accurate than the DEM approach, but significantly more computationally efficient especially at larger geometries. In this paper, we studied fluidized bed heat exchangers up to 7.0 m in diameter and 10.0 m tall; this size is too impractical to use DEM approaches. Therefore, the mathematical description of the CFD model used is described here.

The CFD model solved the conservation of mass, momentum, and energy equations; this allowed for the computation of the pressure, velocity, solid fraction, and temperature distribution within the fluidized bed.

Conservation of mass

The governing volume-averaged conservation of mass equation for both phases, denoted by subscript *l*, is:

$$\frac{\partial \rho_l \alpha_l}{\partial t} + \nabla \cdot (\rho_l \alpha_l \vec{u}) = 0. \tag{A.3.1}$$

The phase volume fraction was constrained by:

$$\sum_{l=1}^{n} \alpha_l = 1, \tag{A.3.2}$$

The gas and solid phases are discrete and there are no chemical reactions present therefore there is no mass source term for each phase.

Conservation of momentum

The volume-averaged conservation of momentum equation for the l^{th} phase is:

$$\frac{\partial(\alpha_l \rho_l \vec{u}_l)}{\partial t} + \nabla \cdot (\alpha_l \rho_l \vec{u}_l \vec{u}_l) = -\alpha_l \nabla p + \nabla \cdot \bar{\bar{\tau}}_l + \alpha_l \rho_l g + \sum_{m=1}^{n} K_{ml}(\vec{u}_m - \vec{u}_l) + S_{mom}. \tag{A.3.3}$$

See below for how the momentum exchange coefficient, K_{ml}, is defined. The momentum source term, S_{mom} for the carrier fluid will include the lift, virtual mass, Brownian and thermophoretic forces. The momentum source term also includes the momentum sink caused by any porous media present as is the case for the particle filter and the solid domain. The component of the momentum sink term for the l^{th} phase in the i^{th} direction due the porous media has the generic form of:

$$S_{l,i} = -\left(\frac{\mu}{\kappa_i} v_{l,i} + \frac{1}{2} C_2 \rho |v| v_{l,i}\right), \tag{A.3.4}$$

In laminar flows, this momentum sink term yields a pressure drop that is consistent with Darcy's Law:

$$\nabla p_l = -\frac{\mu_{g,l}}{\kappa_l} \vec{u}_l. \tag{A.3.5}$$

Conservation of energy

Lastly, the volume-averaged conservation of energy equation for the l^{th} phase is:

$$\frac{\partial(\alpha_l \rho_l E_l)}{\partial t} + \nabla \cdot (\alpha_l \rho_l \vec{u}_l E_l) = -p\left[\frac{\partial \alpha_l}{\partial t} + \nabla \cdot (\alpha_l \vec{u}_l)\right] + \nabla \cdot \left(\alpha_l k_{eff,l} \nabla T_l\right) - h_{ml}(T_l - T_m). \tag{1}$$

Details on the effective thermal conductivity and heat transfer coefficient between phases are described in the Fluent theory manual. No heat source term because no energy source is applied to the fluidized bed other than hot particles enter the PFB HX, where the PFB HX flow and gas/particle heat transfer simulation begin. Unlike a combustion PFB boiler, the PFB HX has no chemical reactions that would form endothermic or exothermic energy sinks or sources, respectively. Interphase momentum and heat exchange follows similar principles as in the MFIX modeling method and can be referred to relevant manual or literatures [40].

Nomenclatures

A	Drag parameter	T	Temperature
A_s	Particle surface area	$\boldsymbol{T}$	Torque vector
B	Drag parameter	u	Velocity
C_p	Specific heat	$\tilde{V}$	Volume
d	Thickness of laminar sub-layer surrounding particle	V_r	Terminal velocities ratio of a group to a single particle
D	Diameter	$\boldsymbol{V}$	Velocity vector
E	Young’s modulus	W	Wedge width
$\boldsymbol{F}$	Force vector	x	Cartesian direction
g	Acceleration due to gravity	$\boldsymbol{X}$	Position vector
$\boldsymbol{g}$	Acceleration vector due to gravity	y	Cartesian direction
h	Local heat transfer coefficient	z	Cartesian direction
$\bar{h}$	Average heat transfer coefficient	*Greeks*	
I	Interphase momentum transfer	α_l	Volume fraction of l^{th} phase
$\boldsymbol{I}$	Momentum vector	β	Momentum transfer coefficient
J	Mass moment of inertia	γ_{cp}	Convective heat transfer coefficient of a particle
k	Spring constant	δ	Particle overlap
K	Function for converting particle drag force to continuum grid	$\boldsymbol{\delta}$	Displacement vector
l	Distance between particle centers	δ_{ij}	Kronecker delta
l_w	Distance between particle surface and wall	ε	Volume fraction
L	Distance from particle center to point of contact	η	Damping coefficient
m	Mass	θ	Surface angle
$\dot{m}$	Mass flow rate	κ	Thermal conductivity
$\dot{m}_z$	Mass flow rate per unit depth	μ	Friction coefficient
Nu	Nusselt number	μ_v	Kinematic viscosity

p	Pressure	μ_g	Dynamic viscosity
$\nabla p^{(i)}$	Pressure gradient at particle position	ν	Poisson’s ratio
Pr	Prandtl number	$\boldsymbol{\xi}$	Unit vector relating particles’ centers
$\dot{Q}$	Heat transfer rate	$\boldsymbol{\xi}'$	Unit vector relating particles’ centers corrected for prolonged contact
r, R	Radius	ρ	Density
R_c	Radius of contact region	τ	Viscous stress tensor
$\tilde{R}_c$	Geometric contact radius	ψ	Volume expansion coefficient
R_f	Upper bound of particle-fluid-particle conduction	$\boldsymbol{\omega}$	Angular velocity vector
s	Minimum conduction distance	$\mathfrak{C}$	The set of particles in contact with a particle
Re	Reynolds number		
t	Time		
Subscripts		Superscripts	
amb	Ambient condition	CV	Control volume
c	Collisional	i	Particle i
CV	Control volume	j	Particle j
g	Gas	w	Wall
i	i^{th} component of a vector	k	Particle k
in	Inlet	$*$	Effective
j	j^{th} component of a vector		
k	Exterior surface of FEA model		
l	l^{th} continuous phase		
m	m^{th} continuous phase		
n	Normal		
nc	Non-collisional		
out	Outlet		
p	Particle		
pg	Particle-gas		
pp	Particle-particle		
pw	Particle-wall		
pfw	Particle-fluid-wall		
pfp	Particle-fluid-particle		
t	Tangential		

Acronyms

ABCC	Air Brayton Combined Cycle
GTCC	Gas Turbine Combined Cycle
CAES	Compressed Air Energy Storage
CSP	Concentrated Solar Power

ETES	Electric Thermal Energy Storage
HX	Heat Exchanger
HRSG	Heat Recovery Steam Generator
LDES	Long Duration Energy Storage
PFB	Pressurized Fluidized Bed
PSH	Pumped Storage Hydropower
TIT	Turbine Inlet Temperature [°C]

Acknowledgments

This work was authored in part by the National Renewable Energy Laboratory, operated by Alliance for Sustainable Energy, LLC, for the U.S. Department of Energy (DOE) under Contract No. DE-AC36-08GO28308. Funding was provided in part by the DOE Advanced Research Projects Agency–Energy (ARPA-E) DAYS Program under Work Authorization Number 18/CJ000/07/05, which is gratefully acknowledged. We thank Dr. Scott Litzelman, Dr. Halle Cheeseman, Dr. Vivien Lecoustre, and Mr. Max Tuttman for their direction and support. The contributions from General Electric Global Research Center, Dr. James Tallman, Dr. Naveenan Thiagarajan, Dr. Doug Hofer, and Dr. Ching-Jen Tang on performance analysis of air-Brayton combined cycle, are acknoledged. Authors thank NREL colleagues, Mark Mehos and Katie Wensuc, for reviewing and editing the manuscript.

The views expressed in the article do not necessarily represent the views of the DOE or the U.S. Government. The U.S. Government retains and the publisher, by accepting the article for publication, acknowledges that the U.S. Government retains a nonexclusive, paid-up, irrevocable, worldwide license to publish or reproduce the published form of this work, or allow others to do so, for U.S. Government purposes.

References

[1] B. Frew, B. Sergi, P. Denholm, W. Cole, N. Gates, D. Levie, R. Margolis, The curtailment paradox in the transition to high solar power systems, Joule. 5 (2021) 1143–1167. https://doi.org/10.1016/j.joule.2021.03.021.

[2] P. Denholm, W. Cole, A.W. Frazier, K. Podkaminer, N. Blair, The Four Phases of Storage Deployment: A Framework for the Expanding Role of Storage in the U.S. Power System, National Renewable Energy Laboratory. NREL/TP-6A20-77480, 2021. https://www.nrel.gov/docs/fy21osti/77480.pdf.

[3] P. Albertus, J.S. Manser, S. Litzelman, Long-Duration Electricity Storage Applications, Economics, and Technologies, Joule. 4 (2020) 21–32. https://doi.org/10.1016/j.joule.2019.11.009.

[4] O. Schmidt, S. Melchior, A. Hawkes, I. Staffell, Projecting the Future Levelized Cost of Electricity Storage Technologies, Joule. 3 (2019) 81–100. https://doi.org/10.1016/j.joule.2018.12.008.

[5] M. De Rosa, O. Afanaseva, A. V. Fedyukhin, V. Bianco, Prospects and characteristics

of thermal and electrochemical energy storage systems, J. Energy Storage. 44 (2021) 103443. https://doi.org/10.1016/j.est.2021.103443.

[6] C. Augustine, N. Blair, Storage Futures Study Storage Technology Modeling Input Data Report Storage Technology Modeling Input Data Report, (2021) 1–84. https://www.nrel.gov/docs/fy21osti/78694.pdf.

[7] C. Forsberg, S. Brick, G. Haratyk, Coupling heat storage to nuclear reactors for variable electricity output with baseload reactor operation, Electr. J. 31 (2018) 23–31. https://doi.org/10.1016/j.tej.2018.03.008.

[8] C.W. Forsberg, Variable and Assured Peak Electricity Production from Base-Load Light-Water Reactors with Heat Storage and Auxiliary Combustible Fuels, Nucl. Technol. 205 (2019) 377–396. https://doi.org/10.1080/00295450.2018.1518555.

[9] D. Enescu, G. Chicco, R. Porumb, G. Seritan, Thermal energy storage for grid applications: Current status and emerging trends, Energies. 13 (2020). https://doi.org/10.3390/en13020340.

[10] Z. Ma, X. Wang, P. Davenport, J. Gifford, J. Martinek, Preliminary Component Design and Cost Estimation of a Novel Electric-Thermal Energy Storage System Using Solid Particles, J. Sol. Energy Eng. 144 (2022) 031001-1–12. https://doi.org/10.1115/1.4053256.

[11] Advanced Research Projects Agency – Energy, Funding Opportunity Announcement Advanced Research Projects Agency – Energy (ARPA-E) DURATION ADDITION TO ELECTRICITY STORAGE (DAYS), 2018.

[12] Z. Ma, G.C. Glatzmaier, C.F. Kutscher, The Thermal Energy Storage Solution, Sol. Today. 26 (2012) 22–26.

[13] Malta Inc., Meet the Future of Energy Storage, an Option to Store Energy on the Grid at Low Cost for Long Durations, (n.d.). https://www.maltainc.com/.

[14] C.S. Turchi, J. Vidal, M. Bauer, Molten salt power towers operating at 600–650 °C: Salt selection and cost benefits, Sol. Energy. 164 (2018) 38–46. https://doi.org/10.1016/j.solener.2018.01.063.

[15] M. Mehos, C. Turchi, J. Vidal, M. Wagner, Z. Ma, C. Ho, W. Kolb, C. Andraka, Z. Ma, A. Kruizenga, NREL, Concentrating Solar Power Gen3 Demonstration Roadmap, Nrel/Tp-5500-67464. (2017) 1–140. https://doi.org/10.2172/1338899.

[16] PFBC Enviromental Energy Technology Inc., How a PFBC System Works, (2018). http://www.pfbceet.com/our-technology/how-a-pfbc-system-works/.

[17] P. Davenport, Z. Ma, W. Nation, J. Schirck, M. Lambert, Thermal Stability of Silica for Application in Thermal Energy Storage, 26th International SolarPACES Conference, September 28 - October 2, 2020, in: 2020.

[18] Covia, Technical Dara Sheet, Granusil Mineral Filler, Wedron, IL, (2021) 1–2.

[19] J. Gifford, Z. Ma, P. Davenport, Thermal Analysis of Insulation Design for a Thermal Energy Storage Silo Containment for Long-Duration Electricity Storage, Front. Energy Res. 8 (2020) 1–12. https://doi.org/10.3389/fenrg.2020.00099.

[20] Z. Ma, J. Gifford, P. Davenport, D. Jia, J. Schirck, A. Morris, Electric Charging Particle Heater for Electric Energy Storage, U.S. Patent Application Number 17/375,105, 2021.

[21] R. Garg, T. Li, S. Pannala, J. Galvin, Documentation of open-source MFIX-DEM software for gas-solids flows, National Energy Technology Laboratory, Morgantown, West Virginia, 2012. https://mfix.netl.doe.gov/documentation/dem_doc_2012-1.pdf.

[22] S. Benyahia, M. Syamlal, T.J. O'Brien, Summary of MFIX Equations 2012-1, National Energy Technology Laboratory, Morgantown, West Virginia, 2012. https://mfix.netl.doe.gov/documentation/MFIXEquations2005-4-4.pdf.

[23] M. Syamlal, W. Rogers, T.J. O'brien, MFIX Documentation Theory Guide Technical Note (DE94000087), National Energy Technology Laboratory, Morgantown, West

Virginia, 1993.

[24] J. Schirck, Z. Ma, A. Morris, Simulations of heat transfer to flowing particles used for long duration thermal energy storage, Submitt. to J. Appl. Therm. Eng. (2021).

[25] Z. Ma, P. Davenport, R. Zhang, Design analysis of a particle-based thermal energy storage system for concentrating solar power or grid energy storage, J. Energy Storage. 29 (2020) 101382. https://doi.org/10.1016/j.est.2020.101382.

[26] Z. Ma, Design of Particle-based Thermal Energy Storage for a Concentrating Solar Power System, in: ASME Power Energy, Charlotte, NC, 2017: pp. 1–8.

[27] Z. Ma, X. Wang, P. Davenport, J. Gifford, J. Martinek, Economic Analysis of an Electric Thermal Energy Storage System Using Solid Particles for Grid Electricity Storage, in: Proc. ASME 2021 15th Int. Conf. Energy Sustain. ES2021 June 16-18, 2021, Virtual, Online, 2021: pp. ES2021-61729 1–10.

[28] U.S. Department of Energy National Energy Technology Laboratory, Tidd PFBC Demonstration Project A DOE Assessment, 2001.

[29] W.-C. Yang, Handbook of Fluidization and Fluid-Particle Systems, Marcel Dekker, Inc., New York, NY, 2003.

[30] PFBC Enviromental Energy Technology Inc., PFBC Competitive Clean Coal Power Utilizing Pressurized Fluidized Bed Combined Cycle Technology, 2018. http://www.pfbceet.com/our-technology/.

[31] GE Power, Powering the World with gas power systems, 2016.

[32] C. Vandervort, D. Leach, M. Scholz, Advancements in H Class Gas Turbines for Combined Cycle Power Plants for High Efficiency, Enhanced Operational Capability, and Broad Fuel Flexibility, in: Futur. Gas Turbine Technol. 8th Int. Gas Turbine Conf., 2016: pp. 1–9.

[33] R.B. Laughlin, Pumped thermal grid storage with heat exchange, J. Renew. Sustain. Energy. 9 (2017) 044103–1. https://doi.org/10.1063/1.4994054.

[34] J. McTigue, P. Farres-Antunez, K. Sundarnath, C. Markides, A. White, Techno-economic analysis of recuperated Joule-Brayton Pumped Thermal Electricity Storage (PTES) systems, Manuscr. Submitt. to Appl. Energy. (2021).

[35] A. Benato, A. Stoppato, Pumped Thermal Electricity Storage: A technology overview, Therm. Sci. Eng. Prog. 6 (2018) 301–315. https://doi.org/10.1016/J.TSEP.2018.01.017.

[36] A. V Olympios, J.D. McTigue, P. Farres-Antunez, A. Tafone, A. Romagnoli, Y. Li, Y. Ding, W.-D. Steinmann, L. Wang, H. Chen, C.N. Markides, Progress and prospects of thermo-mechanical energy storage—a critical review, Prog. Energy. 3 (2021) 022001. https://doi.org/10.1088/2516-1083/abdbba.

[37] R. Garg, J. Galvin, T. Li, S. Pannala, Open-source MFIX-DEM software for gas-solids flows: Part I-Verification studies, Powder Technol. 220 (2012) 122–137. https://doi.org/10.1016/j.powtec.2011.09.019.

[38] T. Li, R. Garg, J. Galvin, S. Pannala, Open-source MFIX-DEM software for gas-solids flows: Part II - Validation studies, Powder Technol. 220 (2012) 138–150. https://doi.org/10.1016/j.powtec.2011.09.020.

[39] M. Syamlal, T.J. O’Brien, Simulation of granular layer inversion in liquid fluidized beds, Int. J. Multiph. Flow. 14 (1988) 473–481. https://doi.org/10.1016/0301-9322(88)90023-7.

[40] D.J. Gunn, Transfer of heat or mass to particles in fixed and fluidised beds, Int. J. Heat Mass Transf. 21 (1978) 467–476. https://doi.org/10.1016/0017-9310(78)90080-7.